Improved regional gravity fields on the Moon from Lunar Prospector tracking data by means of localized spherical harmonic functions

Shin-Chan Han[1,2]

Received 16 April 2008; revised 9 July 2008; accepted 30 July 2008; published 26 November 2008.

[1] An approach to enhance regional gravity fields of the planets using the line-of-sight (LOS) Doppler range-rate measurements is presented. Instead of representing the gravity fields as nonlocalized spherical harmonic functions, I introduced a lumped harmonic representation for obtaining regionally concentrated orthogonal basis functions. Without any regularization or spectral power control, the gravity fields over the four spherical cap regions with the radius of 20° on the nearside of the Moon to degree and order 200 were estimated using all 8 months of the extended mission data from Lunar Prospector. The regional models are variations on the initial global gravity model LP100J. It was found that the regional estimates significantly improve the initial gravity model at all four regions of interest. My improved gravity models fit the LOS Doppler range-acceleration data better than any other global lunar gravity model, especially the data for when the satellite was at low altitude (40 km or less). In addition, a better cross correlation with the topography was obtained from the regional model. The regional enhancement of the correlation was prominent in degrees greater than 100 and in polar regions characterized by clusters of medium- or small-size craters that are presumably uncompensated.

Citation: Han, S.-C. (2008), Improved regional gravity fields on the Moon from Lunar Prospector tracking data by means of localized spherical harmonic functions, *J. Geophys. Res.*, *113*, E11012, doi:10.1029/2008JE003166.

1. Introduction

[2] Earth's and other planets' gravitational and magnetic potential fields have been modeled by analyzing satellite tracking data and measurements from onboard instruments, respectively, using spherical harmonic functions, i.e., solutions of the Laplace equation defined on a sphere. The direct tracking of the lunar-orbiting satellite from Earth is impossible owing to synchronous rotation of the Moon about Earth. The farside of the Moon is covered only by ~20° or less over the limb [*Konopliv et al.*, 2001]. It yields no direct Doppler measurements in the farside of the Moon covering ~40% of the entire surface. Consequently, the modeling of the lunar gravity field with the data gap in the farside with spherical harmonic functions (nonlocalized and global spherical basis functions) has been a challenge. Some kind of empirical regularization by controlling the spectral power of each coefficient (Kaula's law, for example) is mandatory to obtain stable (but biased) solutions when parameterized with those nonlocalized basis functions because the global basis functions are not separable with incomplete coverage of noisy observations.

[3] The power law constraint is equivalent to the assumption that the parameters to be adjusted are a stochastic process defined with the zero mean of each coefficient and the variance following an empirically adopted function, such as scaled $1/l^4$ where l is the spherical harmonic degree. Such power law may be reconciled with the fractal behavior of the gravity field and topography of the planets [*Turcotte*, 1987] and help to prevent the high-degree terms from developing excessive power even with the full tracking data for Mars' and Venus' gravity fields [*Smith et al.*, 1999; *Konopliv et al.*, 1999]. However, its incorporation into the normal equation of the Doppler tracking observations for the gravity analysis obviously introduces bias in the estimates by zero mean assumption. The raw tracking data especially at low altitudes could not be fully exploited in global modeling owing to the farside gap no matter how high in degree and order are modeled, as also noted in the work of *Konopliv et al.* [2001].

[4] The Doppler observation residuals with respect to the global spherical harmonic model of the gravity field are provided from the missions for Venus (Magellan) and the Moon (Lunar Prospector). They can be obtained from the Web site of Planetary Data System (PDS) Geosciences Node (http://pds-geosciences.wustl.edu). In this study, a methodology to improve the regional gravity fields from those Doppler data residuals is explored. The results with Lunar Prospector extended mission data are presented.

[1]Planetary Geodynamics Laboratory, NASA Goddard Space Flight Center, Greenbelt, Maryland, USA.
[2]Also at Goddard Earth Science and Technology Center, University of Maryland Baltimore County, Baltimore, Maryland, USA.

This paper is not subject to U.S. copyright.
Published in 2008 by the American Geophysical Union.

[5] First, I describe how to use the Doppler residual data for regional refinement of the lunar gravity field. The new localized basis functions, originally developed in the work of *Grunbaum et al.* [1982] and further enhanced by *Wieczorek and Simons* [2005], *Simons et al.* [2006], and *Simons and Dahlen* [2006], are introduced to analyze the data. Without any assumption such as power law regularization, those localized basis functions can be used to model the short-wavelength gravity components using a regional subset of the data. Gravity modeling with variable spatial resolutions depending on the sensitivity of tracking data (primarily dependent on altitude) is possible. However, no refined information about the farside gravity field is obtained. The farside gravity is typically constrained by stochastic modeling of global spherical harmonic basis with the nearside observations. I show the enhanced regional gravity fields modeled to degree and order 200 at four regions of the nearside of the Moon and compare the results with the latest global gravity models and also independent topography data.

2. Line-of-Sight Acceleration Residuals

[6] The fundamental observation for gravity analysis from the Lunar Prospector (LP) Mission is a Doppler measurement indicating line-of-sight (LOS) range change over a certain period between the planetary probe and the station on Earth. The range change $\dot{\rho}(t)$ is expressed by

$$\dot{\rho}(t) = \mathbf{v}_{12}(t)^T \mathbf{e}_{12}(t), \tag{1}$$

where $\mathbf{v}_{12}(t)$ is a relative velocity vector of the probe with respect to Earth station and $\mathbf{e}_{12}(t)$ is LOS unit vector (or direction cosines) which is a relative position vector normalized by its length. I introduce a calculated range rate $\tilde{\dot{\rho}}(t)$ from the predicted position and velocity vectors computed on the basis of a priori gravity model. Then, the residual range rate $\delta\dot{\rho}(t)$ is approximated by

$$\delta\dot{\rho}(t) \approx \tilde{\mathbf{v}}_{12}(t)^T \delta\mathbf{e}_{12}(t) + \delta\mathbf{v}_{12}(t)^T \tilde{\mathbf{e}}_{12}(t), \tag{2}$$

where $\delta\dot{\rho}(t) = \dot{\rho}(t) - \tilde{\dot{\rho}}(t)$, $\delta\mathbf{v}_{12}(t) = \mathbf{v}_{12}(t) - \tilde{\mathbf{v}}_{12}(t)$, $\delta\mathbf{e}_{12}(t) = \mathbf{e}_{12}(t) - \tilde{\mathbf{e}}_{12}(t)$, and $\tilde{\mathbf{v}}_{12}(t)$ and $\tilde{\mathbf{e}}_{12}(t)$ are the predicted state vectors. In equation (2), the first order approximation is used. That is, $\delta\mathbf{v}_{12}(t)^T\ \delta\mathbf{e}_{12}(t) = 0$. The equation is further simplified considering the accuracy of Doppler observation which is on the order of 1 mm/s or so. For the extended mission with a low altitude of ~30 km, the velocity vector would be on the order of 1–2 km/s, and the orbit error is around 100 m [*Konopliv et al.*, 2001]. (For the nominal mission with the altitude of ~100 km, the velocity and orbit error decrease greatly and so does the sensitivity of the Doppler measurements to gravity.) The orbit error and Earth-Moon distance give a rough idea about a magnitude of $\delta\mathbf{e}_{12}(t)$ and I get a magnitude of the first term of equation (2) as $\tilde{\mathbf{v}}_{12}(t)^T\ \delta\mathbf{e}_{12}(t) \sim 2 \times 10^3$ m/s $\times \frac{100\,\mathrm{m}}{3.6\times10^8\,\mathrm{m}} \sim 0.5$ mm/s. Note that it would be considerably smaller for the nominal mission data and will be negligible for the other planets. The first term of equation (2), therefore, is expected to be smaller than or within the noise level, and thus equation (2) is reduced to $\delta\dot{\rho}(t) \approx \delta\mathbf{v}_{12}(t)^T\ \tilde{\mathbf{e}}_{12}(t)$ and the successive time derivative yields the following expression:

$$\delta\ddot{\rho}(t) \approx \delta\mathbf{a}_{12}(t)^T \tilde{\mathbf{e}}_{12}(t) + \delta\mathbf{v}_{12}(t)^T \dot{\tilde{\mathbf{e}}}_{12}(t), \tag{3}$$

where $\delta\mathbf{a}_{12}(t) = \partial\delta\mathbf{v}_{12}(t)/\partial t$. The second term of equation (3) is expected as small as 0.01 mGal (10^{-7} m/s^2) since the velocity error of the lunar orbiting satellite is expected on the order of 0.1 m/s on the basis of the orbit computation with various lunar gravity models (D. Rowlands, personal communication, 2008). The temporal change of the LOS direction cosine vector $\dot{\tilde{\mathbf{e}}}_{12}(t)$ is around 10^{-6} s^{-1}. That is, $\delta\mathbf{v}_{12}(t)^T\ \dot{\tilde{\mathbf{e}}}_{12}(t) \sim 0.1$ m/s $\times\ 10^{-6}$ s$^{-1} \sim 10^{-7}$ m/s^2 and it can be neglected considering the observation noise. Finally, I achieve an expression for the LOS residual acceleration given by

$$\delta\ddot{\rho}(t) \approx \delta\mathbf{a}_S(t)^T \tilde{\mathbf{e}}_{12}(t), \tag{4}$$

where the residual relative acceleration vector $\delta\mathbf{a}_{12}(t)$, i.e., the difference between residual acceleration by planet and residual acceleration by Earth, was replaced with the mismodeled acceleration $\delta\mathbf{a}_S(t)$ exerted on the planetary probe by the planetary gravity field. It is valid since he residual acceleration from Earth's gravity is considerably smaller. Any mismodeling of nonconservative force is neglected. Equation (4) implies a linear relationship between the time derivative of the Doppler residuals and the residual gravitational acceleration vector projected onto the (calculated) LOS direction. In addition, the registration error introduced when the acceleration $\delta\mathbf{a}_S(t)$ is evaluated with imperfect orbit is negligible. This model has been used by some researchers to infer high-frequency gravity signatures unmodeled by global geopotential models for Venus [*Kaula*, 1996; *Barriot et al.*, 1998] and for the Moon [*Sugano and Heki*, 2004] but without consideration of a priori orbit accuracy. *McKenzie and Nimmo* [1997] and *Crosby and McKenzie* [2005] computed the admittance directly from the LOS acceleration to infer the elastic thickness for Venus and the Moon, respectively. *Goosens et al.* [2005a, 2005b] showed a short-arc method to obtain the regional gravity field parameterized with the gravity anomalies on the surface grid points from the residual LOS velocity data.

3. Localized Spherical Basis Functions

[7] To analyze the LOS residual acceleration data for a regional gravity field, I employ the basis functions described in the work of *Simons and Dahlen* [2006], i.e., an alternative orthogonal set of spherical and regionally concentrated functions that are called spherical Slepian functions after *Slepian* [1983]. These are based on spherical harmonic expansions and thus satisfy the same differential equation and boundary condition on a sphere, which is different from the spherical cap harmonic basis functions proposed originally by *Haines* [1985] and refined recently by *Thébault et al.* [2006]. These spherical Slepian functions are built from linear combinations of standard spherical harmonic functions. They have some advantages for certain

applications of planetary gravity modeling. Particularly, they are ideal when an inversion is being done from data with uneven coverage or with uneven sensitivity owing to high eccentricity.

[8] I start by defining a band-limited signal $s(\theta, \lambda)$ on a sphere in terms of the usual spherical harmonic basis and in terms of the alternative set of Slepian basis functions as follows:

$$s(\theta, \lambda) = \sum_{l=0}^{L} \sum_{m=-l}^{l} u_{lm} Y_{lm}(\theta, \lambda) = \sum_{n=1}^{(L+1)^2} v_n g_n(\theta, \lambda), \qquad (5)$$

where θ and λ are colatitude and longitude, respectively. Y_{lm} (θ, λ) and g_n (θ, λ) are the spherical harmonic function of degree l and order m and the n-th Slepian function, respectively. u_{lm} and v_n are the spherical harmonic and Slepian expansion coefficients, respectively. L is the maximum degree of spherical harmonic expansion. The Slepian basis function g_n (θ, λ) is also expressed by spherical harmonic basis as follows:

$$g_n(\theta, \lambda) = \sum_{l=0}^{L} \sum_{m=-l}^{l} g_{n,lm} Y_{lm}(\theta, \lambda). \qquad (6)$$

That is, the n-th Slepian function is determined on the basis of spherical harmonic functions with the expansion coefficient of $g_{n,lm}$. Note that there exist $(L + 1)^2$ number of alternative basis functions which are mutually orthogonal and span the same vector space constructed by the same number of usual spherical harmonic basis functions.

[9] The spherical harmonic coefficient $g_{n,lm}$ of the new basis function g_n (θ, λ) is determined by maximizing the ratio between its energy within a given area Ω and the energy within the entire globe, such as

$$\gamma_n = \int_{\Omega} g_n^2(\theta, \lambda) d\Omega \Big/ \int_0^{2\pi} \int_0^{\pi} g_n^2(\theta, \lambda) \sin\theta d\theta d\lambda, \qquad (7)$$

where Ω is a subset of a sphere and γ_n is the power ratio indicating the quality of spatial concentration of the function g_n (θ, λ) in the region. The maximization problem can be solved in a spectral domain via the eigen problem as discussed in the work of *Grunbaum et al.* [1982] and *Simons and Dahlen* [2006]. In a straightforward way, all necessary γ_n and $g_{n,lm}$ are obtained from the eigenvalue and eigenvector, respectively, with given information about the region such as latitude and longitude bounds for irregular region or the center location and radius of spherical cap for an isotropic region. Note that the dimension of eigenvector is $(L + 1)^2$ and there are total $(L + 1)^2$ orthogonal eigenvectors $g_{n,lm}$ and eigenvalues γ_n.

[10] Combining equation (5) and (6), the relationship between the spherical harmonic coefficients u_{lm} and Slepian coefficients v_n can be found as follows:

$$v_n = \sum_{l=0}^{L} \sum_{m=-l}^{l} u_{lm} g_{n,lm}. \qquad (8)$$

Also considering the orthogonality of eigenvectors ($\sum_{l=0}^{L} \sum_{m=-l}^{l} g_{n',lm}\, g_{n,lm} = \delta_{nn'}$, where $\delta_{nn'} = 1$ if $n = n'$, otherwise $\delta_{nn'} = 0$), the following is obtained:

$$u_{lm} = \sum_{n=1}^{(L+1)^2} v_n g_{n,lm}. \qquad (9)$$

By introducing a new variable, γ_0, I separate equation (9) into two terms, $u^{\circ}{}_{lm}$ and $u_{lm}^{\perp}$, defined by

$$u_{lm}^{\circ} = \sum_{n=1}^{N} v_n g_{n,lm} \text{ with } \gamma_n \geq \gamma_0 \text{ for } n = 1, 2, \ldots, N, \qquad (10a)$$

$$u_{lm}^{\perp} = \sum_{n=N+1}^{(L+1)^2} v_n g_{n,lm} \text{ with } \gamma_n < \gamma_0 \text{ for } n = N+1,\ N+2,\ \ldots, (L+1)^2. \qquad (10b)$$

They satisfy $u_{lm} = u_{lm}^{\circ} + u_{lm}^{\perp}$. The quantity g_n (θ, λ) with γ_n close to 1 represents the basis function concentrated within the region of interest (and v_n is the corresponding coefficient), while $g_n(\theta, \lambda)$ with γ_n close to 0 is the complementary one concentrated outside the region of interest. Provided $\gamma_0 = 0.1$, for example, u_{lm}° represents the contribution mostly from the region of interest and thus is called localized coefficients. $u_{lm}^{\perp}$ includes the other contribution from the complementary region on the sphere. The geographical separation of global spherical harmonic coefficients can be done in this way. An operation computing u_{lm}° from u_{lm} is hereafter referred to as localization of the global coefficients.

[11] In summary, as an entire set (regionally concentrated ones and their complementary), the Slepian functions represent gravity over the entire planet. With the choices of (1) a maximum degree L to which spherical harmonics will be used, (2) a subset area of the planet, and (3) a cutoff (tolerance) concentration, there is a well-defined procedure to find all possible linear combinations of spherical harmonic functions (up to degree L) that have a power ratio greater than the specified cutoff over the specified subset area. Suppose that with the degree specified at L, N spherical Slepian functions with the power ratio greater than the tolerance are found for the region. As with standard spherical harmonics, when an inversion is made using these spherical Slepian functions, one estimates the coefficients (multipliers) of the functions. If the specified area has good data coverage, then the orthogonality of the basis functions helps ensure that the coefficients of the N basis functions that have their power concentrated in the specified area will be especially well determined and not receive any degradation from areas with poor coverage.

[12] As an example, I focus on a spherical cap region with the radius of 20° (~600 km on the Moon's surface) and set $\gamma_0 = 0.0001$ (to include all possible basis yielding 0.0001 or greater power ratio) and seek for band-limited basis functions with the maximum degree and order of 200. There are 201^2 orthogonal functions but only 1585 functions (N = 1585) yield the concentration ratio greater than γ_0. The rest of the functions are concentrated on the complementary

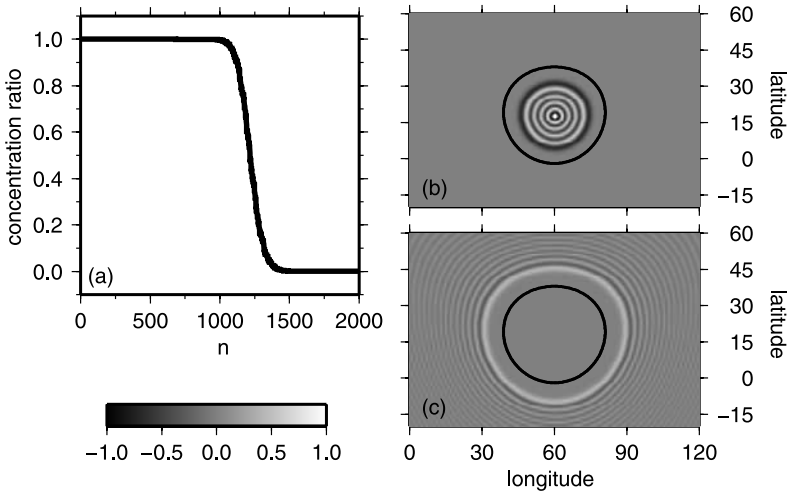

Figure 1. (a) Concentration ratios of the first 2000 Slepian harmonic basis functions, sorted by the ratio in a descending order. Here n indicates the function number. There are 201^2 orthogonal harmonic functions to span a band-limited ($L_{\max} = 200$) vector space, but only 1585 functions are concentrated with the ratio greater than 0.0001 within the spherical cap area depicted by the black circle in Figures 1b and 1c. The examples of well-concentrated basis functions (b) inside the region and (c) outside the region are shown after normalization. Note that both functions are global-support, harmonic, orthogonal, and expanded using usual spherical harmonic functions to degree and order 200.

region. The gravity signal (up to degree and order of 200) in the region can be effectively modeled using only 1585 well-concentrated functions g_n (θ, λ) with $n \leq N$ or $\gamma_n \geq \gamma_0$. Figure 1a shows concentration ratio γ_n for $n \leq 2000$ and γ_n for $2001 \leq n \leq 201^2$ (not shown) is smaller than 10^{-10}. Figures 1b and 1c present examples of two basis functions, including the one concentrated within the spherical cap region and the other in the complementary region. The boundary of the cap area is depicted in a black circle. The well-concentrated basis shown in Figure 1b yields a concentration ratio greater than 0.999999, while the one in Figure 1c yields 10^{-30}.

[13] I show an illustration of geographical separation of the global gravity field by means of regional basis functions. Figure 2a presents the radial gravity component on a sphere with a radius of 1738 km from the LP150Q model [*Konopliv et al.*, 2001] to degree and order 30, which reflects the long-wavelength component and thus is less accurately represented with the regionally concentrated basis functions. The positive gravity anomalies, negatively correlated with topography over the Mare Crisium area (mass concentration, mascon) [*Muller and Sjogren*, 1968], are known to be due to mantle uplift and/or higher-density material such as mare basalts [*Neumann et al.*, 1996; *Wieczorek and Phillips*, 1999; *Konopliv et al.*, 2001]. The black circle divides the sphere into two subset regions. Most of the new basis functions are concentrated either inside or outside of the circular region as indicated by the sharp drop of concentration ratio in Figure 1a. Figure 2b shows the high-pass filtered gravity signal (degree and order between 31 and 150) from LP150Q, which are decomposed into the regionally concentrated basis functions. First, I compute the Slepian coefficients v_n using equation (8) from the band-pass filtered LP150Q coefficients. Then I compute two sets of spherical harmonic coefficients, u°_{lm} and $u^{\perp}_{lm}$, using equation (10a) and (10b), respectively.

[14] Figures 2c and 2d show the radial gravity from u°_{lm} and $u^{\perp}_{lm}$, respectively. The combination of both maps, Figures 2c and 2d, is exactly equal to the map shown in Figure 2b. (Note that both coefficients u°_{lm} and $u^{\perp}_{lm}$ define the field on the entire globe, but shown only a rectangular region.) Clearly, one set of coefficients, u°_{lm}, represents the anomaly inside of the region while the other set, $u^{\perp}_{lm}$, models the anomaly outside of the region. The error committed by representing the inside anomaly with Slepian basis is computed by differencing 2(c) and 2(b) and is evaluated only inside the region. It is generally as small as <1 mGal (<0.5%) within the inner most spherical cap with a radius of 18° (note that the cap size is 20°). The error near the cap boundary (at radius of 18°–20°) is as large as 1–3 mGal owing to more significant influence by excluding complementary basis or by truncating the Slepian basis to N.

[15] The accuracy of the localized representation u°_{lm} of regional anomaly depends on a wavelength of the signal to be represented with regional basis functions as well as the total number of basis functions, N (or threshold γ_0). In Figure 2, I represent the band-pass signal ($31 \leq l, m \leq 150$) with the Slepian basis functions. The representation error grows gradually as more low-degree harmonic components are included in the regional decomposition. For example, if I use the gravity signals from degree 9 which is the longest wavelength that can be completely sampled within the cap with a radius of 20°, the error grows to several mGal (as opposed to a few 0.1 mGal if I use the signals from degree 30). If the entire signals from degree 2 are used, the regional representation and global spherical harmonic representation differ by some tens mGal and spurious long-wavelength features are created in the regional representation. There-

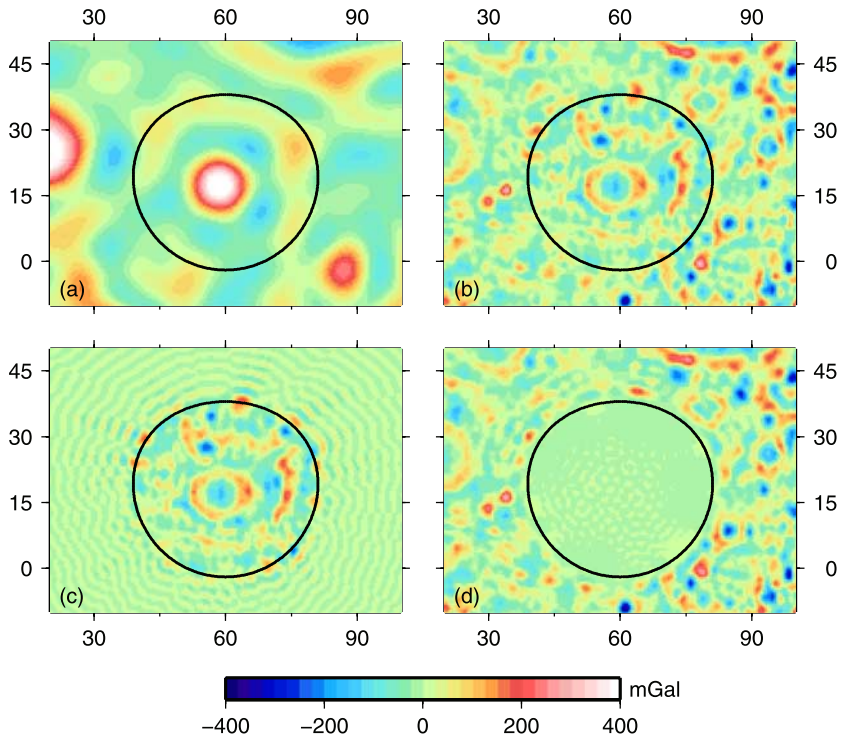

Figure 2. (a) Low-pass filtered (l, $m \leq 30$) radial gravity component of LP150Q evaluated on the reference sphere. (b) Same as Figure 2a, but high-pass filtered ($31 \leq l$, $m \leq 150$) radial gravity. (c) Same as Figure 2b, but only using well-concentrated Slepian basis functions. (d) Same as Figure 2b, but only using complementary basis functions. Note that the sum of Figures 2c and 2d is exactly equal to Figure 2b within machine precision.

fore, I will analyze the gravity fields higher than degree 30, which guarantees sub mGal accuracy in the regional representation and rely on the a priori global harmonic field for the components smaller than degree 30.

[16] For implementing the Slepian basis function to the observation equation given in equation (4) and using equation (9), I express the acceleration vector $\delta\mathbf{a}_S(r, \theta, \lambda)$ acting on the satellite as follows:

$$\delta\mathbf{a}_S(r,\theta,\lambda) = \sum_{n=1}^{(L+1)^2} \delta\mathbf{a}_S^n(r,\theta,\lambda), \tag{11a}$$

$$\delta\mathbf{a}_S^n(r,\theta,\lambda) = \frac{GM}{R}\sum_{l=0}^{L}\sum_{m=-l}^{l} v_n g_{n,lm} \cdot \left(\begin{bmatrix} \dfrac{\partial}{\partial r} \\ \dfrac{\partial}{r\partial\theta} \\ \dfrac{\partial}{r\sin\theta\partial\lambda} \end{bmatrix} \left(\frac{R}{r}\right)^{l+1} Y_{lm}(\theta,\lambda)\right), \tag{11b}$$

where $\delta\mathbf{a}_S^n(r, \theta, \lambda)$ is a component of the acceleration vector associated with n-th Slepian basis. GM is the multiplication of gravitational constant and the planet's total mass. R is a reference radius of the spherical harmonic expansion. For the regional analysis, the contribution from the complementary region is neglected. That is, I truncate the upper bound of equation (11a) to N. Putting equation (11a) and (11b) to (4),

$$\delta\ddot{\rho}(t) = \tilde{\mathbf{e}}_{12}(t)^T \sum_{n=1}^{N} \delta\mathbf{a}_S^n(r,\theta,\lambda) = \sum_{n=1}^{N} v_n \cdot \left\{ \frac{GM}{R}\sum_{l=0}^{L}\sum_{m=-l}^{l} g_{n,lm} \left(\tilde{\mathbf{e}}_{12}(t)^T \begin{bmatrix} \dfrac{\partial}{\partial r} \\ \dfrac{\partial}{r\partial\theta} \\ \dfrac{\partial}{r\sin\theta\partial\lambda} \end{bmatrix} \left(\frac{R}{r}\right)^{l+1} Y_{lm}(\theta,\lambda) \right) \right\}. \tag{12}$$

It is an expression of linear observation equation for the Slepian coefficient parameters v_n and LOS acceleration observations $\delta\ddot{\rho}(t)$. After solving for the parameters, the free-air gravity anomaly and equipotential surface with respect to the mean sphere are computed as follows:

$$\delta g(\theta,\lambda) = \sum_{n=1}^{N} v_n \frac{GM}{R}\sum_{l=0}^{L}\sum_{m=-l}^{l} g_{n,lm}\left(\frac{l+1}{R}\right) Y_{lm}(\theta,\lambda), \tag{13a}$$

$$\delta N(\theta,\lambda) = \sum_{n=1}^{N} v_n R \sum_{l=0}^{L}\sum_{m=-l}^{l} g_{n,lm} Y_{lm}(\theta,\lambda). \tag{13b}$$

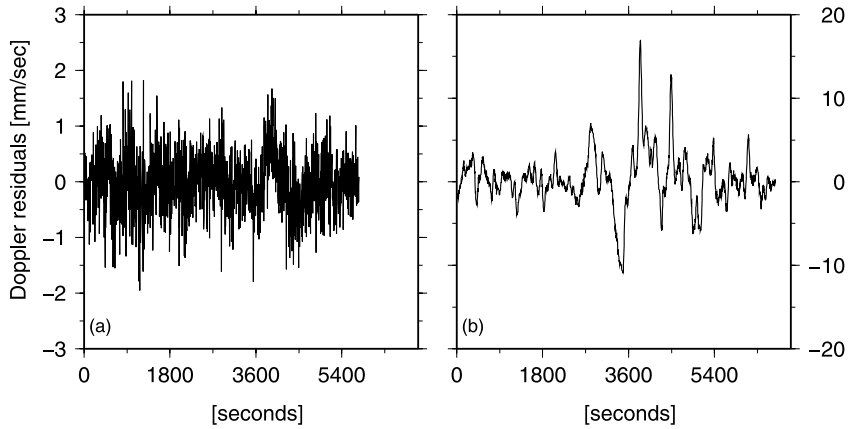

Figure 3. Doppler range-rate residuals (the observed range rate with respect to the calculated one with LP100J for lunar gravity model). (a) Nominal mission data at altitude of ~100 km, PDS data ln02186j. (b) Extended mission data at altitude of ~30 km, PDS data lx01421j.

[17] The evaluation of (13a) and (13b), however, is valid only within the region of interest, for example, inside of the spherical cap, simply owing to the fact that I do not solve the gravity field in the complementary region by truncating the upper bound in equation (11a).

4. Doppler Residual Data From the Lunar Prospector Mission

[18] In this section, I overview the data used for enhanced regional gravity recovery. The LP orbit and Doppler residuals data are provided from PDS Geosciences Node. I analyzed the data archived under the Line of Sight Acceleration Profile Data Record (http://pds-geosciences.wustl.edu/missions/lunarp/los.html) and acquired during the extended mission period from 19 December 1998 to 30 July 1999.

[19] For example, Figure 3 shows the Doppler residuals for one orbital revolution in the middle of the nominal mission period with the altitude of ~100 km and of the extended mission with the altitude of ~30 km. The residuals indicate only lunar gravitational perturbations beyond the a priori model LP100J because other gravitational and nongravitational effects were already removed from the raw Doppler measurements by the orbit computations when the residuals were generated (A. Konopliv, personal communication, 2008). The residuals during the nominal mission are generally as small as several 0.1 mm/s except long-wavelength components in the level of 1 mm/s. Notably, the residuals during the extended mission retain significant perturbations exceeding 10 mm/s from the unmodeled and mismodeled gravity fields which were less sensitive to the data collected at the higher altitude during the nominal mission. On the other hand, it is expected that the instrument noise level is more or less the same for both extended and nominal missions and thus a comparison between the two data sets will indicate the overall noise level of the tracking data.

[20] Figure 4a presents the square root of power spectral density (PSD) for the residual Doppler range-rate data. The nominal and extended mission data are depicted in light red

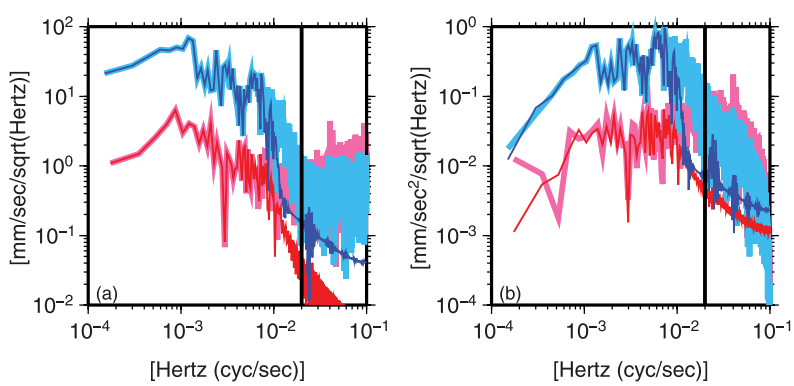

Figure 4. Square root of power spectral density (PSD) of (a) range-rate residual and (b) its time derivative; that is, range acceleration or LOS acceleration. The red and blue colors denote nominal and extended mission data, respectively. The thick and thin lines indicate the raw data and PDS-provided smoothed version, respectively. My range-acceleration residuals, depicted by thick lines in Figure 4b, are derived from a cibic B-spline fit and the successive (analytic) time derivatives. The derived range acceleration is damped when the frequency is greater than the critical frequency, 0.02 Hz (50 s per period), marked with a vertical line.

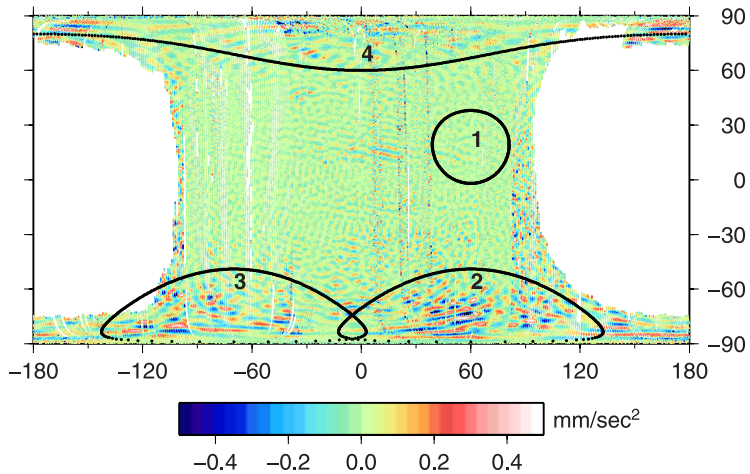

Figure 5. LOS acceleration from the last 300 revolutions of the extended data. The four spherical cap regions used in this study are depicted in the black circles (labeled 1–4). All occupy the same surface area with a cap radius of 20°. There is a large data gap in the farside with a cap radius of ~75°.

and light blue with thicker line, respectively. The PSD of the spline fit provided by PDS Geosciences Node was also drawn in red and blue color (thin line) for nominal and extended mission data, respectively. Assuming that both data contain similar amount of instrumental noise, the spectral bandwidth in which the noise dominates is found to be 0.02 Hz or higher, also indicated by a black vertical line in the figure. In this band, the noise seems to be in the level of ~1 mm/sec/$\sqrt{\text{Hz}}$. The PDS-provided data fit (thin line) diminishes the useful signals contained in the bandwidth of 0.01 Hz to 0.02 Hz, caused by too conservative smoothing, which is also noted by *McKenzie and Nimmo* [1997]. Consequently, I do not use the data fit from the PDS, but use the raw Doppler residual data.

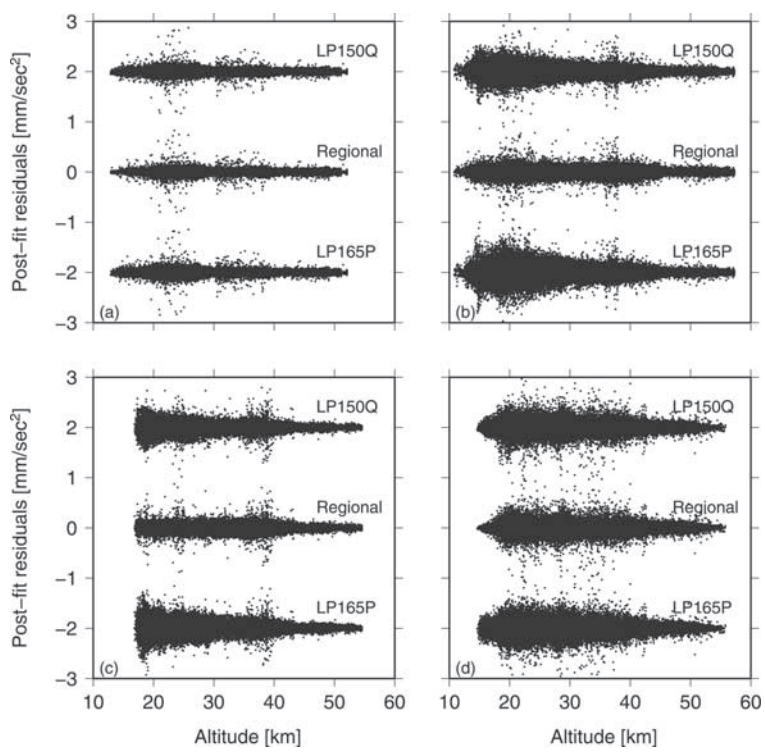

Figure 6. Postfit residuals of LOS acceleration over (a) region 1, around Mare Crisium; (b) region 2, centered at 69S/60E; (c) region 3, centered at 69S70W; (d) region 4, around the North Pole. The postfit residuals were computed using two global models, LP150Q (L_{max} = 150) and LP165P (L_{max} = 165), and the regional model (L_{max} = 200) with Slepian basis. For clearer plots, arbitrary values were added for LP150Q and LP165P residuals. The average altitudes at each region for the entire extended mission period are 31, 32, 32, and 32 km.

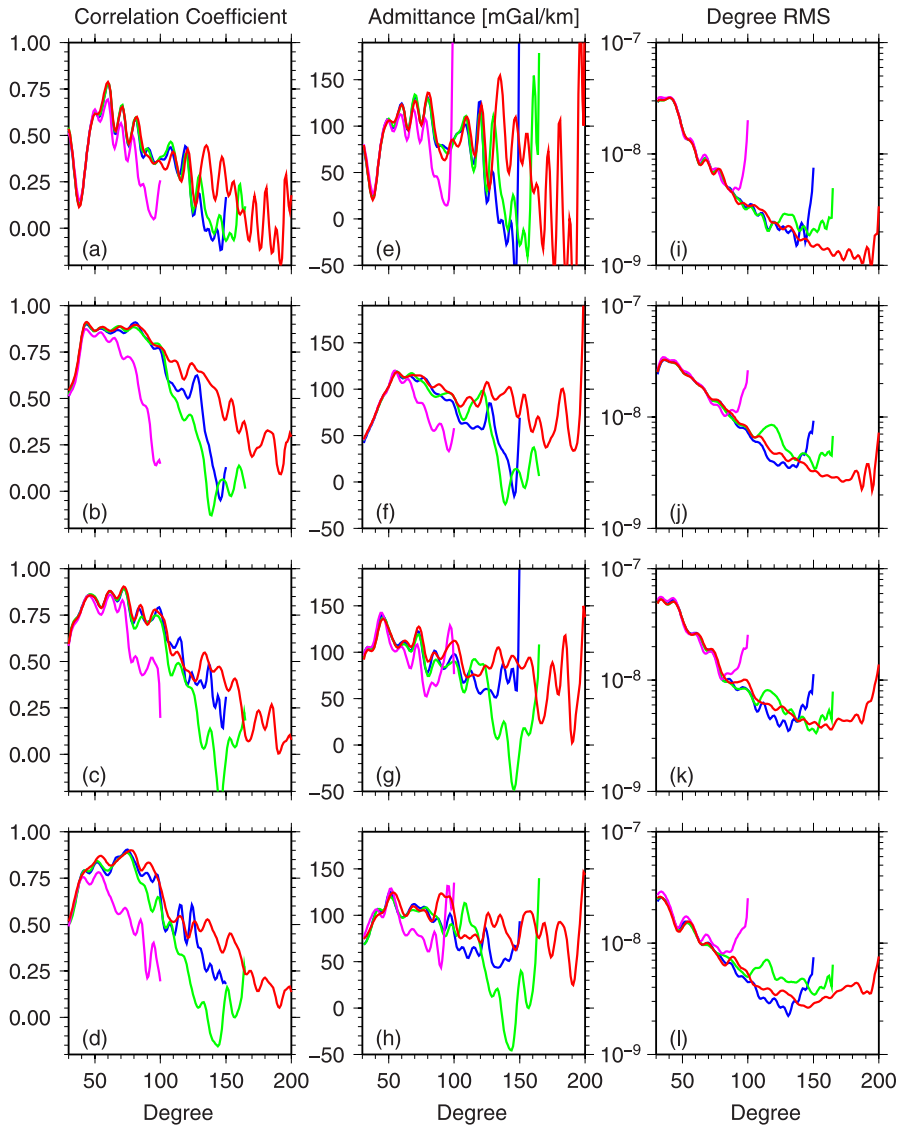

Figure 7. (a)–(d) Cross correlation between gravity and topography over the four regions. The regional correlations after localizing the global gravity and topography models in each region were computed from degree 31 to the maximum degrees for the respective gravity models including LP100J (magenta), LP150Q (blue), and LP165P (green). The correlation of topography with the regional gravity model was shown in red line. (e)–(h) The admittance functions. (i)–(l) The degree RMS curves.

[21] In order to compute the LOS acceleration, I performed the cubic B-spline [*de Boor*, 1978] fit to the Doppler residuals and obtained the time derivative analytically from the cubic B-spline model to compute the range acceleration. To account for amplification of the noise by differentiation, I applied the low-pass (or high-cut) filter by damping the spectral components greater than 0.02 Hz with a factor $(f_0/f)^2$, where $f_0 = 0.02$ Hz and $f > f_0$. The PSD of smoothed derivative of Doppler residual data is given in Figure 4b. As already implied by Doppler residuals, the PDS computed LOS acceleration is too smooth so that the gravity signal between 0.01 Hz and 0.02 Hz is filtered out. In my LOS acceleration data, the noise, expected to be amplified by differentiation, at the frequency greater than 0.02 Hz is suppressed by the applied smoothing (low-pass) filter and is around several 0.01 mm/sec$^2/\sqrt{\text{Hz}}$ (or some mGal/$\sqrt{\text{Hz}}$).

[22] Analyzed are the entire Doppler residual data every 5 s (sometimes 10 s) for the extended mission period from 19 December 1998 to 30 July 1999. During this period, the altitude (with respect to the sphere with a radius of 1738 km) varied from 10 km to 55 km with an average of 30 km which roughly corresponds to the "rule-of-thumb" sensitivity to degree and order 200 for the Moon. (Also note that the mean altitude varies depending on the location on the Moon) Figure 5 shows the LOS acceleration (my smoothed one) for the last 23 days of the extended mission amounting to a total 300 revolutions. Some regions are producing particularly large perturbations indicating where the gravity field is comparatively not well modeled by the a

Table 1. Cross Correlation Between the Lunar Topography and the Gravity Models in Various Spherical Harmonic Degree Bands[a]

Gravity Model	R1	R2	R3	R4
	Degree Band 31–100			
LP100J	0.38	0.65	0.67	0.56
LP150Q	0.48	0.82	0.78	0.78
LP165P	0.48	0.82	0.78	0.75
Regional	0.48	0.83	0.79	0.80
	Degree Band 101–150			
LP150Q	0.18	0.41	0.44	0.39
LP165P	0.21	0.29	0.24	0.18
Regional	0.31	0.62	0.50	0.49
	Degree Band 151–165			
LP165P	0.05	0.04	0.09	0.09
Regional	0.15	0.39	0.31	0.37
	Degree Band 166–200			
Regional	0.02	0.24	0.13	0.16

[a]R1 through R4 indicate the regions depicted in Figure 5.

priori model LP100J. I selected four spherical cap regions with a cap radius of 20°, centered at (1) 18N/60E including Mare Crisium, (2) 69S/60E, (3) 69S/70W, and (4) 80N/0E. Except (1), the gravity fields in other regions are suspected to be ill determined or to not fully incorporate the low-altitude measurements since they produce larger gravitational perturbations in the LOS acceleration residuals. The mean altitude of the satellite in the four regions for the entire extended mission period was 31 km, 32 km, 32 km, and 32 km, respectively. Therefore the large perturbations in certain regions are likely due to the inherently rich short-wavelength gravity signals rather than variable mean altitudes. Note that the polar region of the lunar surface is characterized by many small and intermediate craters (radius smaller than 150 km) which may create short-wavelength gravity signals yielding positive correlation with uncompensated topography possibly owing to lithospheric rigidity [*Turcotte et al.*, 1981].

[23] In each region, a normal matrix is accumulated using all extended mission data in the region on the basis of a linear equation given in (12). The equal weighting for all data is applied. No attempt was made to scale the weights posteriorly. A least squares inversion is performed for the Slepian coefficients v_n without any regularization. The number of regional basis functions, well concentrated in each region with the concentration ratio greater than 0.0001 and extended to degree and order of 200, is 1585 which is 25 times smaller than the number of necessary spherical harmonic basis functions, 40401(=201^2). The numbers of observations are 71155, 210289, 205233, and 296217 for the regions 1, 2, 3, and 4, respectively.

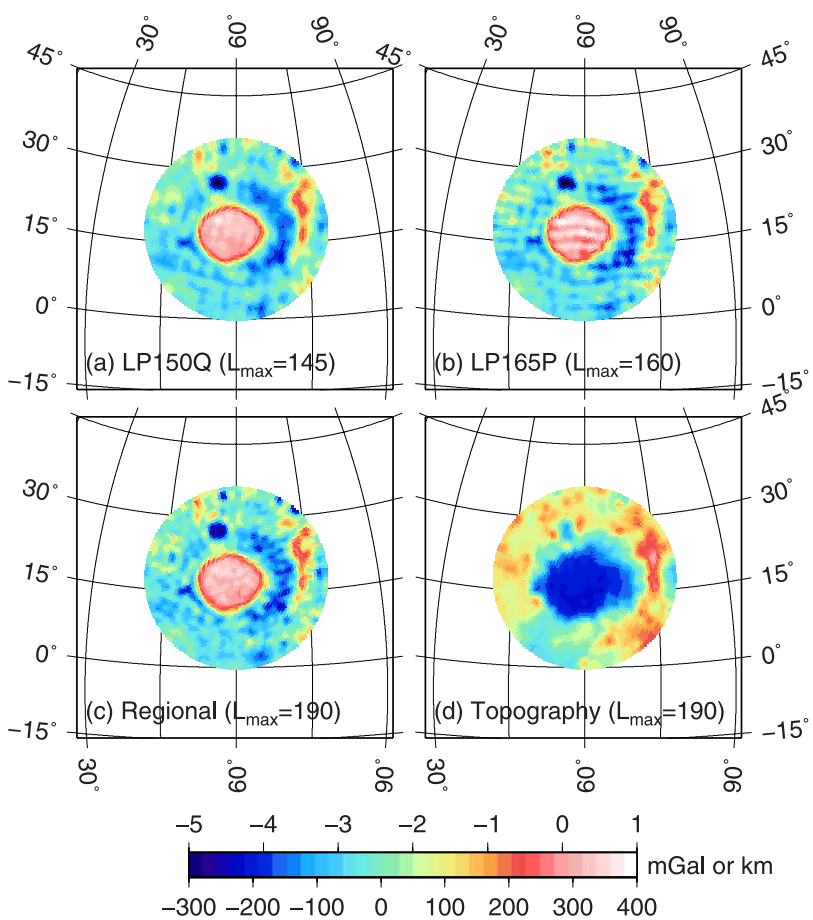

Figure 8. The radial component of the gravity vector evaluated on the reference sphere over the region 1 from (a) LP150Q, (b) LP165P, and (c) the regional model. (d) The topography map is also shown for comparison.

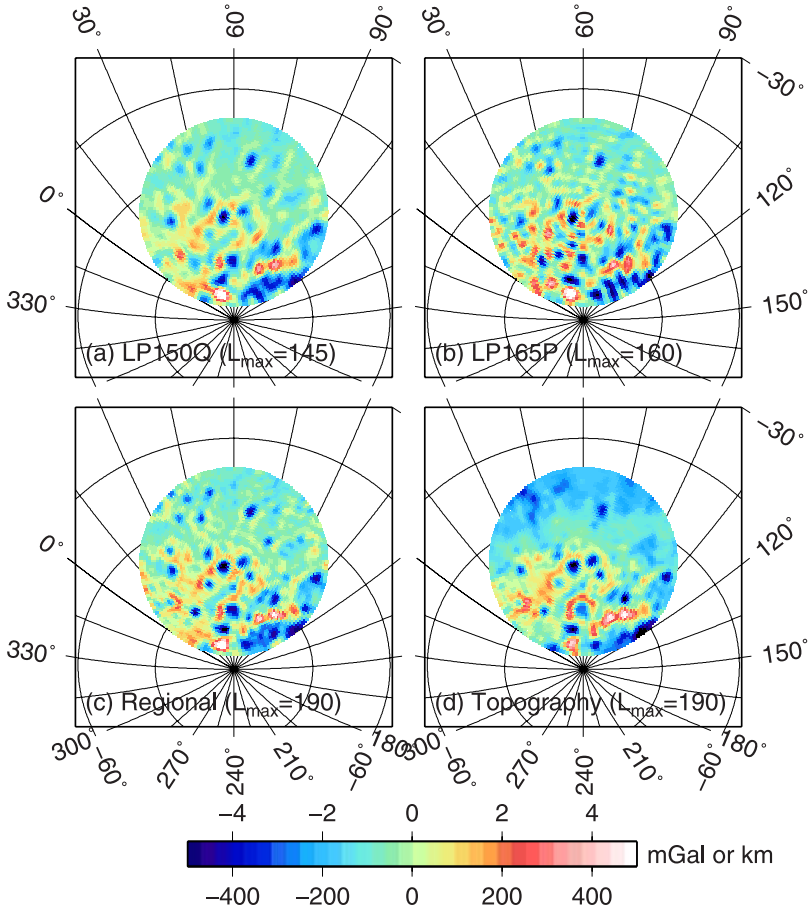

Figure 9. Same as in Figure 8, but over region 2.

[24] After estimating the Slepian coefficients, the postfit residuals were computed in the four regions as shown in Figure 6. The initial standard deviation of the LOS residual acceleration data (with respect to LP100J model) was 6.87, 12.28, 10.57, and 9.64 mGal in the four regions, respectively. It was reduced with the latest models including LP150Q and LP165P in all the regions. The postfit residuals with LP150Q are smaller than the ones with LP165P. However, the regional gravity fields modeled with the Slepian basis function produces the smallest postfit residuals for all the cases. For the region 1, the standard deviation of the postfit residuals from LP150Q, LP165P, and the regional model is 5.12, 5.23, and 4.63 mGal, respectively. For the region 2, it is 8.04, 10.60, and 5.95 mGal, respectively. For the region 3, it is 7.15, 9.15, and 5.24 mGal, respectively. For the region 4, it is 7.82, 9.18, and 6.82 mGal, respectively. The improvement from the regional gravity fields is most significant near the south pole (the regions 2 and 3). The performance of the regional models to fit the LOS acceleration residuals is especially better at the low altitude (lower than 40 km). Neither of LP150Q nor LP165P global model is superior in fitting the LOS acceleration data to the regional model for all the cases.

[25] I also extended the regional basis to degree and order 250 to test possible further reduction of the data particularly at lowest altitudes. The improvement was marginal and the postfit residuals were still larger at an altitude between 20 km to 40 km than between 40 km to 55 km as also found with the regional basis expanded to 200. I suspect the orbits near the limb regions are in particular poorly determined so that the error in deriving the LOS acceleration observation equation (discussed in section 2) is no longer negligible. At lower altitudes near the lunar limb, the Deep Space Network (DSN) S-band signal experiences additional noise owing to multiple reflections (multipath) from the lunar surface. In general, the regional models give the better fit to the data, however it does not necessarily indicate better gravity models. In the next section, independent topography data are used for addressing the quality of the regional gravity models and two other global models.

5. High-Resolution Regional Gravity Fields and Comparison With Topography

[26] In order to assess the gravity models independently, I compared the regional and global gravity estimates with the topography model derived from the USGS Unified Lunar Control Network [*Archinal et al.*, 2006]. Although the topography data may also yield errors on the order of km (some 100 mGal in gravity assuming uncompensated topography and crustal density) in certain regions, the comparison between the gravity and topography data may be the unique way to assess the quality of both data at the moment. The global topography of the Lunar surface will be significantly improved with the near-future mission, Lunar

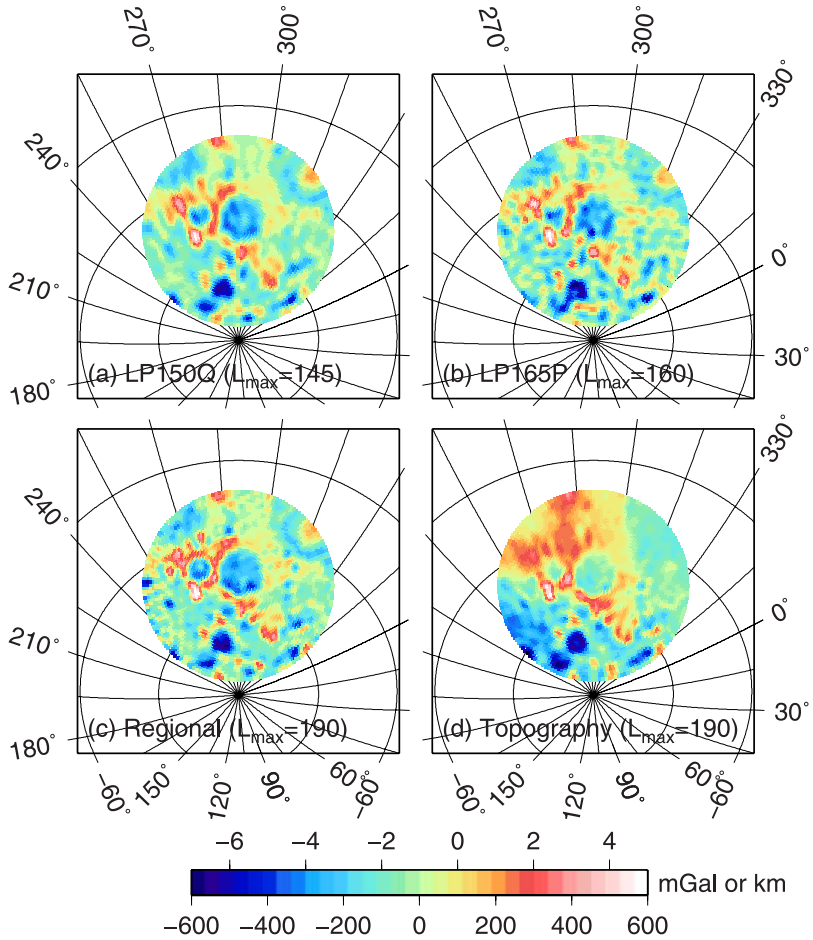

Figure 10. Same as in Figure 8, but over region 3.

Reconnaissance Orbiter (LRO) [*Chin et al.*, 2007]. The spherical harmonic coefficients of the topography data [*Archinal et al.*, 2006] were expanded to degree and order 359 [*Wieczorek*, 2007] and are available via the Web site (http://www.ipgp.jussieu.fr/∼wieczor/SH/SH.html). The degree correlation and admittance functions between the gravity and topography are given as

$$C(l) = \frac{\sum_{m=0}^{l} \left\{ C_{lm}^{grav} C_{lm}^{topo} + S_{lm}^{grav} S_{lm}^{topo} \right\}}{\sqrt{\sum_{m=0}^{l} \left\{ \left(C_{lm}^{grav}\right)^2 + \left(S_{lm}^{grav}\right)^2 \right\}} \sqrt{\sum_{m=0}^{l} \left\{ \left(C_{lm}^{topo}\right)^2 + \left(S_{lm}^{topo}\right)^2 \right\}}}, \tag{14a}$$

$$A(l) = \frac{\sum_{m=0}^{l} \left\{ C_{lm}^{grav} C_{lm}^{topo} + S_{lm}^{grav} S_{lm}^{topo} \right\}}{\sum_{m=0}^{l} \left\{ \left(C_{lm}^{topo}\right)^2 + \left(S_{lm}^{topo}\right)^2 \right\}}, \tag{14b}$$

where C_{lm}^{grav} and S_{lm}^{grav} are the gravity field coefficients (note that they are scaled by $(l + 1)/R$ to the potential field coefficients) and C_{lm}^{topo} and S_{lm}^{topo} are the topography coefficients.

[27] Equation (8) shows that the Slepian coefficient is nothing but lumped spherical harmonic coefficients, and the estimated Slepian coefficients are easily transformed back to the spherical harmonic coefficients using equation (10a). The transformed spherical harmonic coefficients would represent the "residual" regional gravity field with respect to LP100J and be valid only inside the cap area. In order to get the full regional signature, the LP100J coefficients were added, but degrees and orders higher than 30, to the regional coefficient estimates after expanding the LP100J coefficients (from degree 31 to 150) using the Slepian basis functions with $\gamma \leq \gamma_0$. The combined coefficients essentially represent the band-limited regional gravity field. The low-degree components (degrees less than 30) are not intended to be improved by the regional estimates, because the subset of data (not global data) would not constrain the low-degree harmonics well.

[28] After localizing the topography coefficients in the same way, the degree correlation and admittance were computed in each region using equation (14a) and (14b). Figures 7a–7d show degree correlations between topography and various gravity models at the four regions, Region 1 through 4, respectively. The regional correlations of localized global gravity fields, LP100J (magenta), LP150Q (blue), and LP165P (green) with topography at

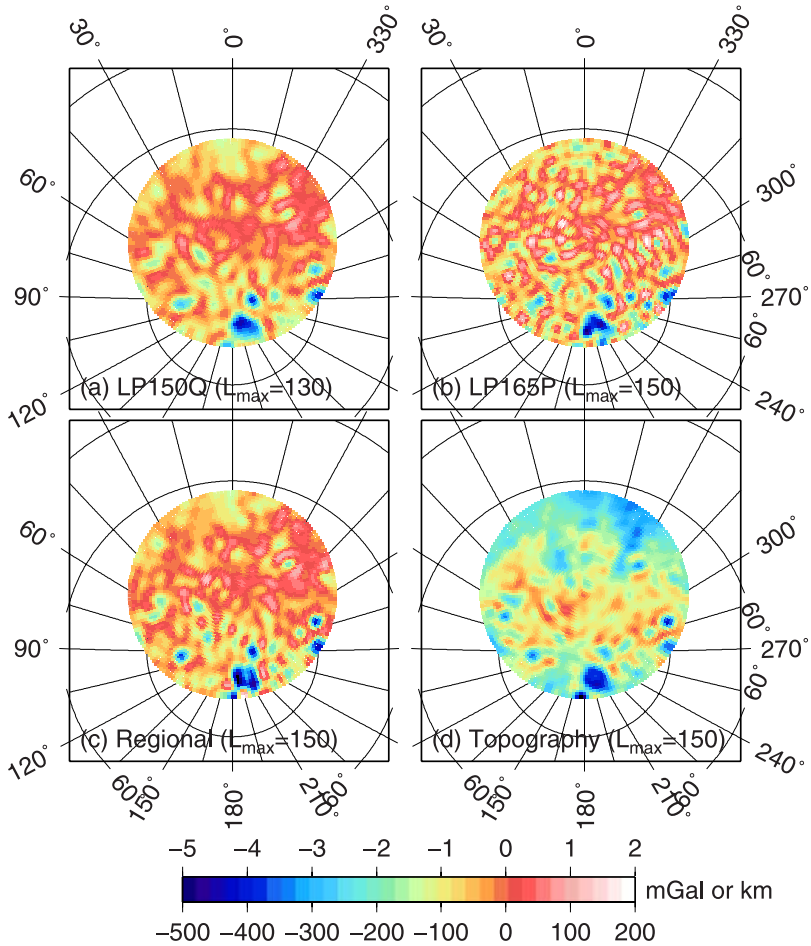

Figure 11. Same as in Figure 8, but over region 4.

various regions were compared with the correlations of regional Slepian gravity solutions (red) from degree 31 to the maximum degrees of the respective models.

[29] Over the Mare Crisium, the regional correlations of all gravity fields with topography are smaller than at other regions. It may be due to the higher-density mare material that creates anticorrelated gravity, although the majority of such mascon effect is eliminated by suppressing low-degree harmonics (l, $m \leq 30$). The small and intermediate craters with fewer mascon signatures dominate over the polar region and thus a better correlation of the gravity with topography is expected since the topography is likely uncompensated by flexural rigidity of the lunar crust [*Arkani-Hamed*, 1998]. All gravity models (localized) in the polar region show higher correlations than the global average correlation. In all areas of interest, the correlation is improved by refining the a priori gravity field LP100J (magenta) with the regional gravity field estimates (red). The significant improvement starts from degree 50 or so. Also the regional gravity model is correlated with topography better than any other global model (either LP150Q or LP165P), especially in higher degrees (l, $m \geq 100$ or so). In Table 1, the correlations among the models averaged within the degree bands of 31–100, 101–150, 151–165, and 166–200 were computed separately to compare the gravity models along the spherical harmonic degrees. In all bands, the regional models show the largest correlation with the topography.

[30] The gravity improvement by regional refinement is also evident from the admittance curves depicted in Figures 7e–7h. The admittance from the regional models tends to converge to a constant ~100 mGal/km or so, which essentially implies the (uncompensated) lithospheric density, at higher degrees better than other (localized) global models. Alternatively, *Wieczorek and Simons* [2005, 2007] explored the methods to compute localized correlation and admittance functions from the (nonlocalized) global spherical harmonic representation of the gravity and topography fields with the examples from Mars [*McGovern et al.*, 2002; *Belleguic et al.*, 2005].

[31] The energy spectra are compared by computing the degree RMS per degree and order given as

$$S(l) = \sqrt{\sum_{m=0}^{l} \left(C_{lm}^2 + S_{lm}^2\right)/(2l+1)}. \qquad (15)$$

It reflects the degree-wise variability of each coefficient. Figures 7i–7l present the regional degree RMS from LP100J (magenta), LP150Q (blue), and LP165P (green), after localization at each region, and from the regional Slepian gravity model (red). The localized power is largest

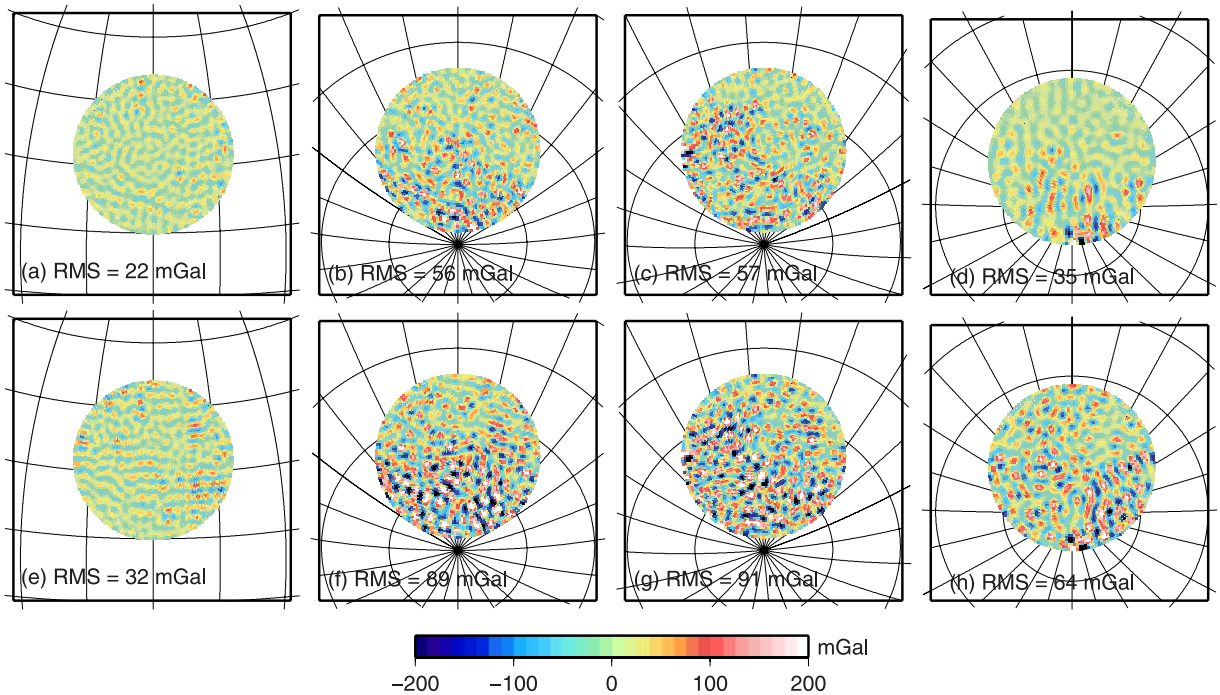

Figure 12. The gravity differences (a)–(d) between LP150Q and the regional models and (e)–(h) between LP165P and the regional models for the four spherical cap regions. Figures 12a and 12e, Figures 12b and 12f, Figures 12c and 12g, and Figures 12d and 12h are the same areas depicted in Figures 8, 9, 10, and 11, respectively.

at the regions close to South pole indicating that high-frequency gravity signatures induced by cluster of the craters. The increasing power close to the Nyquist degree from each model seems to be due to noise and aliasing caused by unmodeled high-frequency signals. I, therefore, evaluated the gravity models to the degrees and orders before the power increases. For example, the LP150Q, LP165P, and the regional Slepian models were evaluated to 145, 160, and 190, respectively, at the first three regions and 130, 150, and 150 at the region 4. For minimizing the edge effects, I do not use the gravity information near the boundary of the spherical cap of each region. That is, the region was originally defined by the center location and cap radius of 20°, but the regional coefficients are evaluated only within the inner most cap with a radius of 18° (See also Figure 2 and the associated paragraph).

[32] Figures 8–11 show the radial gravity maps, computed following equation (13a) or its equivalent for global coefficients, at four regions using LP150Q, LP165P, and the regional model (refined from LP100J). Note that, for the gravity map from the regional model, the low-degree coefficients (l, $m \leq 30$) were fixed with a priori model LP100J and only high-degree coefficients from 31 to 200 were refined by the regional analysis. The topography map is also shown for comparison. Although the regional gravity model shows clear improvement from the initial model LP100J, for the Mare Crisium region, it is hard to judge whether the regional model is actually better than the model LP150Q. It is difficult to assess the gravity against the topography since the region is characterized with the mascon diminishing the correlation of the gravity field with topography. The LP165P model produces spurious zonal patterns in the gravity anomalies.

[33] However, over the southern hemisphere regions (regions 2 and 3; Figures 9 and 10) near the pole, the regional gravity shows clear improvement against any other global model yielding enhanced correlation with topography dominated by the (uncompensated) craters. The cluster of circular and negative gravity anomalies with a diameter of ~90 km (or ~3° in latitude) and the positive anomalies at the surrounding rim around the center of the cap (Figure 9) are well correlated with the crater topography and suggest the admittance of ~100 mGal/km. These gravity features are most delineated from the regional model. The Bailly crater, that is located at 66.5S and 69.1W with a diameter of ~300 km, and smaller craters in the west and southwest shown in Figure 10 are most clearly identified with the regional gravity model. These craters seem to yield higher admittance than the smaller craters in Figure 9. Over the north pole, the regional gravity fields produce the most delineated features for the craters comparable with the ones in topography map, including the ones close to the farside of the Moon. As predicted from the improved degree correlation between the regional gravity and topography, the finer scale of gravity variations of the craters and rims are better resolved by the regional analysis.

[34] The differences of the regional gravity models from the global models including LP150Q and LP165P were shown in Figure 12. The root mean square (RMS) of differences varies from 22 mGal to 91 mGal, depending on the model and region. The largest differences are found in the regions 2 and 3 where the regional gravity models

show most significant improvement in correlation with topography. In all cases, LP165P shows larger difference from the regional models than LP150Q does.

6. Summary

[35] I discussed an useful methodology to enhance short-wavelength gravity signals retained in the Doppler residual data of the Lunar Prospector extended mission. My proposed method is based on the analysis of LOS acceleration residuals with localized spherical basis functions. Those basis functions can be resolved using a regional set of data without any kind of regularization or spectral power control. The LOS acceleration observation equation requires a priori orbit information as accurate as ~100 m to fully account for the Doppler tracking data with accuracy of ~1 mm/s or less for the lunar gravity analysis. However, for the analysis of other planets (such as Venus and Mars), the error caused by the orbit error would be much smaller owing to a greater distance from Earth. The alternative basis functions are simply lumped spherical harmonic functions and thus the transformation to spherical harmonic coefficients is straightforward. It is also possible to model the regional gravity fields with various resolutions depending on the mean altitude of the planetary probe in the region.

[36] The results based on LP extended mission data in the four different areas on the nearside of the Moon show significant enhancement of the short-wavelength gravity signatures by the regional analysis. The regional estimates extracted richer gravity information out of the Doppler residual data especially at low altitude (40 km or below) which were not well exploited by the global gravity model. The improvement was also evident when the regional gravity was assessed with the independent topography data especially over the areas characterized with small and intermediate size craters. In this study, I focused on describing the enhanced regional gravity fields and their assessment. In the future, it will be possible to interpret them for new insights associated with the lunar surface and lithospheric structures as studied in the work of *Neumann et al.* [1996] and *Wieczorek and Phillips* [1998, 1999] for example.

[37] This paper has argued that the global gravity field can be modeled using the raw Doppler shift data by implementing the alternative basis functions (both regionally concentrated one and its complementary) in the dynamic equation for the orbit and gravity analysis. Its advantage over the ubiquitous spherical harmonic representation is that the nearside of lunar gravity field can be estimated without introducing a bias such as stochastic constraint. It will be also possible to construct the nearside gravity field to a higher resolution (higher degrees and orders) and the farside gravity with a low resolution simultaneously.

[38] The analysis discussed in this study can be extended to process the data from near-future lunar missions such as Lunar Reconnaissance Orbiter (LRO) and Gravity Recovery And Interior Laboratory (GRAIL). The regional analysis of the Doppler residual data from Mars Reconnaissance Orbiter (MRO) and Magellan is expected to improve Mars and Venus gravity fields, respectively. It may characterize better the intense regional gravity signatures over the areas such as Olympus, Ascraeus, and Arsia Mons for Mars (some thousands of mGal in gravity) and Atla and Beta Regio for Venus. Finally, it is anticipated that this method will be useful to analyze the tracking data from the probes of highly eccentric orbits with variable resolutions dependent on altitudes, such as MESSENGER to be orbiting around Mercury in 2011 and possibly NEAR orbiting around the asteroid Eros.

[39] **Acknowledgments.** This work was partially supported by the NASA Earth Surface and Interior program and Gravity Recovery And Climate Experiment project. David Rowlands, Frank Lemoine, and Gregory Neumann are acknowledged for their helpful comments on an earlier version of this paper. Alex Konopliv is acknowledged for information about the Lunar Prospector data available from PDS Geosciences node (http://pds-geosciences.wustl.edu). I thank Mark Wieczorek, Francis Nimmo, and an anonymous reviewer for constructive reviews. I acknowledge an anonymous reviewer for the comment on increased S-band measurement error when the spacecraft was orbiting near the limb.

References

Archinal, B. A., M. R. Rosiek, R. L. Kirk, and B. L. Redding (2006), The unified lunar control network 2005, *U.S. Geol. Surv. Open File Rep. 2006–1367*. (Available at http://pubs.usgs.gov/of/2006/1367.)

Arkani-Hamed, J. (1998), The lunar mascons revisited, *J. Geophys. Res.*, *103*, 3709–3739, doi:10.1029/97JE02815.

Barriot, J. P., N. Vales, G. Balmino, and P. Rosenblatt (1998), A 180th degree and order model of the Venus gravity field from Magellan line-of-sight residual Doppler data, *Geophys. Res. Lett.*, *25*, 3743–3746, doi:10.1029/98GL02600.

Belleguic, V., P. Lognonné, and M. Wieczorek (2005), Constraints on the Martian lithosphere from gravity and topography data, *J. Geophys. Res.*, *110*, E11005, doi:10.1029/2005JE002437.

Chin, G., et al. (2007), Lunar Reconnaissance Orbiter overview: The instrument suite and mission, *Space Sci. Rev.*, *129*, 391–419, doi:10.1007/s11214-007-9153-y.

Crosby, A., and D. P. McKenzie (2005), Measurements of the elastic thickness under ancient lunar terrain, *Icarus*, *173*, 100–107, doi:10.1016/j.icarus.2004.07.017.

de Boor, C. (1978), *A Practical Guide to Splines*, 392 pp., Springer, New York.

Goossens, S., P. N. A. M. Visser, and B. A. C. Ambrosius (2005a), A method to determine regional lunar gravity fields from Earth-based satellite tracking data, *Planet. Space Sci.*, *53*, 1331–1340, doi:10.1016/j.pss.2005.06.009.

Goossens, S., P. N. A. M. Visser, K. Heki, and B. A. C. Ambrosius (2005b), Local gravity from Lunar Prospector tracking data: Results for Mare Serenitatis, *Earth Planets Space*, *57*, 1127–1132.

Grunbaum, F. A., L. Longhi, and M. Perlstadt (1982), Differential operators commuting with ?nite convolution integral operators: Some non-Abelian examples, *SIAM J. Appl. Math.*, *42*, 941–955.

Haines, G. V. (1985), Spherical cap harmonic analysis, *J. Geophys. Res.*, *90*, 2583–2591, doi:10.1029/JB090iB03p02583.

Kaula, W. M. (1996), Regional gravity fields on Venus from tracking of Magellan cycles 5 and 6, *J. Geophys. Res.*, *101*, 4683–4690, doi:10.1029/95JE02296.

Konopliv, A. S., W. B. Banerdt, and W. L. Sjogren (1999), Venus gravity: 180th degree and order model, *Icarus*, *139*, 3–18, doi:10.1006/icar.1999.6086.

Konopliv, A. S., S. W. Asmar, E. Carranza, W. L. Sjogren, and D. N. Yuan (2001), Recent gravity models as a result of the Lunar Prospector Mission, *Icarus*, *150*, 1–18, doi:10.1006/icar.2000.6573.

McGovern, P. J., S. C. Solomon, D. F. Smith, M. T. Zuber, M. Simons, M. A. Wieczorek, R. J. Phillips, G. A. Neumann, O. Aharonson, and J. W. Head (2002), Localized gravity/topography admittance and correlation spectra on Mars: Implications, for regional and global evolution, *J. Geophys. Res.*, *107*(E12), 5136, doi:10.1029/2002JE001854.

McKenzie, D., and F. Nimmo (1997), Elastic thickness estimates for Venus from line of sight accelerations, *Icarus*, *130*, 198–216, doi:10.1006/icar.1997.5770.

Muller, P. M., and W. L. Sjogren (1968), Mascons: Lunar mass concentrations, *Science*, *161*, 680–684, doi:10.1126/science.161.3842.680.

Neumann, G. A., M. T. Zuber, D. E. Smith, and F. G. Lemoine (1996), The lunar crust: Global structure and signature of major basins, *J. Geophys. Res.*, *101*, 16,841–16,863, doi:10.1029/96JE01246.

Simons, F. J., and F. A. Dahlen (2006), Spherical Slepian functions and the polar gap in geodesy, *Geophys. J. Int.*, *166*, 1039–1061, doi:10.1111/j.1365-246X.2006.03065.x.

Simons, F. J., F. A. Dahlen, and M. A. Wieczorek (2006), Spatiospectral localization on the sphere, *SIAM Rev.*, *48*, 504–536, doi:10.1137/S0036144504445765.

Slepian, D. (1983), Some comments on Fourier-analysis, uncertainty and modeling, *SIAM Rev.*, *25*, 379–393, doi:10.1137/1025078.

Smith, D. E., et al. (1999), The gravity field of Mars: Results from Mars Global Surveyor, *Science*, *286*, 94–97, doi:10.1126/science.286.5437.94.

Sugano, T., and K. Heki (2004), Isostasy of the Moon from high-resolution gravity and topography data: Implication for its thermal history, *Geophys. Res. Lett.*, *31*, L24703, doi:10.1029/2004GL022059.

Thébault, E., J. J. Schott, and M. Mandea (2006), Revised spherical cap harmonic analysis (R-SCHA): Validation and properties, *J. Geophys. Res.*, *111*, B01102, doi:10.1029/2005JB003836.

Turcotte, D. L. (1987), A fractal interpretation of topography and geoid spectra on the Earth, Moon, Venus, and Mars, *J. Geophys. Res.*, *92*, E597–E601, doi:10.1029/JB092iB04p0E597.

Turcotte, D. L., R. J. Willemann, W. F. Haxby, and J. Norberry (1981), Role of membrane stresses in the support of planetary topography, *J. Geophys. Res.*, *86*, 3951–3959, doi:10.1029/JB086iB05p03951.

Wieczorek, M. A. (2007), Gravity and topography of the terrestrial planets, *Treatise Geophys.*, *10*, 165–205, doi:10.1016/B978-044452748-6/00156-5.

Wieczorek, M. A., and R. J. Phillips (1998), Potential anomalies on a sphere: Applications to the thickness of the lunar crust, *J. Geophys. Res.*, *103*, 1715–1724, doi:10.1029/97JE03136.

Wieczorek, M. A., and R. J. Phillips (1999), Lunar multiring basins and the cratering process, *Icarus*, *139*, 246–259, doi:10.1006/icar.1999.6102.

Wieczorek, M. A., and F. J. Simons (2005), Localized spectral analysis on the sphere, *Geophys. J. Int.*, *162*, 655–675, doi:10.1111/j.1365-246X.2005.02687.x.

Wieczorek, M. A., and F. J. Simons (2007), Minimum-variance multitaper spectral estimation on the sphere, *J. Fourier Anal. Appl.*, *13*, doi:10.1007/s00041-006-6904-1.

S.-C. Han, Planetary Geodynamics Laboratory, Code 698, NASA Goddard Space Flight Center, Greenbelt, MD 20771, USA. (shin-chan.han@nasa.gov)